1997

Atmospheric correction of visible to middle-infrared EOS-MODIS data over land surfaces: Background, operational algorithm and validation

E. F. Vermote
University of Maryland

N. El Saleous
University of Maryland

C. O. Justice
University of Maryland

Y. J. Kaufman
Goddard Space Flight Center

J. L. Privette
Goddard Space Flight Center

See next page for additional authors

JOURNAL OF GEOPHYSICAL RESEARCH, VOL. 102, NO. D14, PAGES 17,131–17,141, JULY 27, 1997

Atmospheric correction of visible to middle-infrared EOS-MODIS data over land surfaces: Background, operational algorithm and validation

E. F. Vermote,[1] N. El Saleous,[1] C. O. Justice,[1] Y. J. Kaufman,[2] J. L. Privette,[2] L. Remer,[3] J. C. Roger,[4] and D. Tanré[5]

Abstract. The NASA moderate resolution imaging spectroradiometer (MODIS) instrument will provide a global and improved source of information for the study of land surfaces with a spatial resolution of up to 250 m. Prior to the derivation of various biophysical parameters based on surface reflectances, the top of the atmosphere signals need to be radiometrically calibrated and corrected for atmospheric effects. The present paper describes in detail the state of the art techniques that will be used for atmospheric correction of MODIS bands 1 through 7, centered at 648, 858, 470, 555, 1240, 1640, and 2130 nm, respectively. Previous operational correction schemes have assumed a standard atmosphere with zero or constant aerosol loading and a uniform, Lambertian surface. The MODIS operational atmospheric correction algorithm, reported here, uses aerosol and water vapor information derived from the MODIS data, corrects for adjacency effects and takes into account the directional properties of the observed surface. This paper also describes the operational implementation of these techniques and its optimization. The techniques are applied to remote sensing data from the Landsat Thematic Mapper (TM), the NOAA advanced very high resolution radiometer (AVHRR), and the MODIS airborne simulator (MAS) and validated against ground-based measurements from the Aerosol Robotic Network (AERONET).

1. Introduction

The use of MODIS data for retrieval of land parameters, such as the bidirectional reflectance distribution function (BRDF), albedo, vegetation indices (VIs), fraction of absorbed photosynthetically active radiation (FPAR), and leaf area index (LAI), requires that the top of the atmosphere radiance be converted to surface reflectance. The process necessary for that conversion is called atmospheric correction. By applying the proposed algorithms and associated processing code, moderate resolution imaging spectroradiometer (MODIS) level 1B radiances are corrected for atmospheric effects to generate the surface reflectance product. Atmospheric correction requires inputs that describe the variable constituents that influence the signal measured at the top of the atmosphere (see Figure 1 and Tables 1a and 1b) and a correct modeling of the atmospheric scattering and absorption (i.e., a band absorption model and multiple-scattering vector code). In addition, an accurate correction requires a correction for the atmospheric point spread function (for high spatial resolution bands) and coupling of the surface BRDF and atmosphere effects.

Over the past few years, considerable effort has been put into the modeling of atmospheric effects at the Laboratoire d'Optique Atmospherique of Lille, France. Recently, the Second Simulation of the Satellite Signal in the Solar Spectrum (6S) radiative code was released [*Vermote et al.*, 1997] and is well suited for various remote sensing applications and is fully documented. It includes simulation of the effects of the atmospheric point spread function and surface reflectance directionality. We are currently using the 6S code as the reference to enable intercomparison of algorithms and to verify the correct implementation of the MODIS atmospheric correction algorithm. For example, Tables 1a and 1b illustrate the application of the code to show the relative atmospheric effects on examples of existing environmental sensors.

Our plan is to use MODIS atmospheric products and ancillary data sets as inputs to the operational atmospheric correction. Collaboration in the area of aerosol retrieval has already been initiated with the MODIS aerosol group [*Kaufman et al.*, this issue]. An important aspect of the operational algorithm is to accommodate the large amount of input data and the necessary fast turnaround of products, without compromising the science objectives or the accuracy goals.

2. Theoretical Background

The surface reflectance product will be computed from the MODIS calibrated radiance data (level 1B) in bands 1 through 7 (centered at 648, 858, 470, 555, 1240, 1640, and 2130 nm, respectively). The product is an estimate of the surface spectral reflectance for each band as it would have been measured at ground level if there were no atmospheric scattering or absorption. The correction scheme includes corrections for the effect of atmospheric gases, aerosols, and thin cirrus clouds, and it is

[1]Department of Geography, University of Maryland and NASA Goddard Space Flight Center, Greenbelt, Maryland.
[2]NASA Goddard Space Flight Center, Greenbelt, Maryland.
[3]Science, System and Applications Inc., NASA Goddard Space Flight Center, Greenbelt, Maryland.
[4]Laboratoire de Physique Appliquée aux Milieux Oceaniques Côtiers, Station Marine-Université du Littoral, France.
[5]Laboratoire d'Optique Atmosphérique, Université des Sciences et Techniques de Lille, Villeneuve d'Ascq, France.

Paper number 97JD00201.
0148-0227/97/97JD-00201$09.00

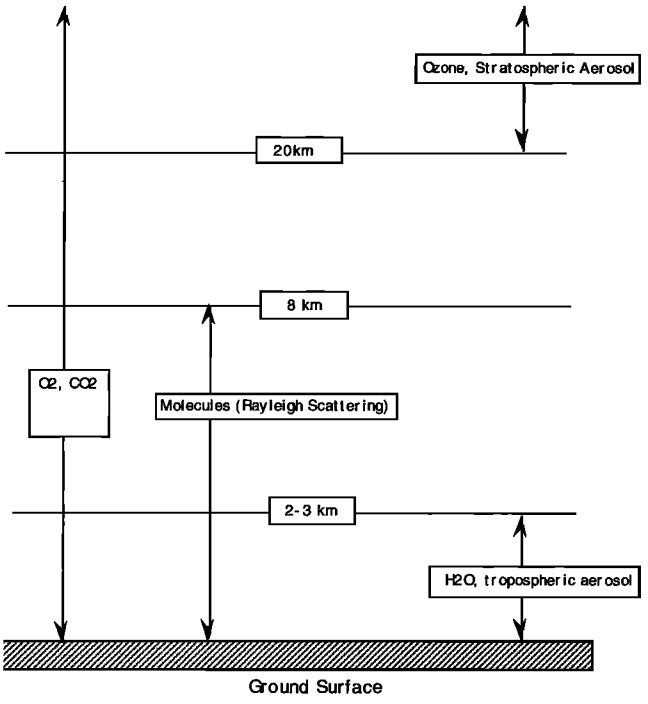

Figure 1. Description of the components affecting a satellite remote sensing signal in the 0.4–2.5 μm range.

applied to all noncloudy level 1B pixels that pass the level 1B quality control. The surface reflectance product is the input for generation for several land products: Vegetation Indices (VIs), BRDF/albedo, thermal anomaly, snow/ice, and FPAR/LAI. Therefore it is an important and essential product. The at-launch version will be fully operational. An Algorithm Theoretical Background Document (ATBD) for the surface reflectance product and the approach adopted for atmospheric correction of MODIS data [*Vermote et al.*, 1995] is available on Home Page of the EOS Science Project Office (SPO) (http://eospso.gsfc.nasa.gov/atbd/pg1.html, ATBD-MOD08).

Rather than reproducing the ATBD contents, this paper focuses on several important and recent improvements to the algorithm, namely, the atmospheric point spread function correction and an atmosphere BRDF coupling correction. One critical aspect of MODIS algorithm development is the need to optimize the algorithm for efficient global processing. In the sections that follow, the practical aspects of global data processing for the algorithm are described.

2.1. Atmospheric Point Spread Function Correction

The case of nonuniform ground boundary conditions has been addressed by several researchers [*Tanré et al.*, 1981; *Kaufman*, 1982; *Mekler and Kaufman*, 1980]. The correction approach is to assume that the signal received by the satellite is a combination of the reflectance of the target pixel and reflectances from surrounding pixels, each weighted by their distance from the target. Because the apparent signal at the top of the atmosphere of a pixel comes also from adjacent pixels, this effect is also called adjacency effect. The correction involves inverting the linear combination of reflectances to solve for the reflectance of the target pixel.

We present here the proposed operational implementation. It should be noted that this effect will be less important for MODIS with a 250–500 m pixels than it is for higher spatial resolution data, for example, 30 m pixel from Thematic Mapper. The correction procedure stems from the modeling work by *Tanré et al.* [1981] and is simplified in this code for operational application.

In the case of an infinite uniform Lambertian target of reflectance ρ_s^u, the reflectance at the top of the atmosphere, ρ_{TOA} could be written as

$$\rho_{\mathrm{TOA}} = \rho_{R+A} + \frac{\rho_s^u T_{R+A}(\mu_s) T_{R+A}(\mu_v)}{1 - \rho_s^u S_{R+A}}. \quad (1)$$

Table 1a. Order of Magnitude of Atmospheric Effects for AVHRR Bands 1 and 2 and NDVI = (Band 2 − Band 1)/(Band 2 + Band 1)

	Ozone 0.247–0.480, cm/atm	Water Vapor 0.5–4.1, g/cm^2	Rayleigh, 1013 mbar	Aerosol V: 60–10 km Continental
ρ_1 620 ± 120 nm	4.2–12%	0.7–4.4%	0.02–0.06	0.005–0.12
ρ_2 885 ± 195 nm	···	7.7–25%	0.006–0.02	0.003–0.083
NDVI (bare soil) ρ_1 = 0.19, ρ_2 = 0.22	0.02–0.06	0.011–0.12	0.036–0.094	0.006–0.085
NDVI (deciduous forest) ρ_1 = 0.03 ρ_2 = 0.36	0.006–0.017	0.036–0.038	0.086–0.23	0.022–0.35

The proportional effect (transmission) is given as percentage (%) of increase ( ) or reduction ( ) of the signal. All other effects as well as the effect on the normalized difference index (NDVI) are given in absolute units; ρ_1 is the reflectance observed in the advanced very high resolution radiometer (AVHRR) band 1; ρ_2 is the reflectance observed in AVHRR band 2.

Table 1b. Order of Magnitude of Atmospheric Effects for TM Bands 1–5 and 7 and NDVI = (Band 4 − Band 3)/(Band 4 + Band 3)

	Ozone 0.247–0.480, cm/atm	Water Vapor 0.5–4.1, g/cm^2	Rayleigh, 1013 mbar	Aerosol V: 60–10 km Continental
ρ_1 490 ± 60 nm	1.5–2.9%	···	0.064–0.08	0.007–0.048
ρ_2 575 ± 75 nm	5.2–13.4%	0.5–3%	0.032–0.04	0.006–0.04
ρ_3 670 ± 70 nm	3.1–7.9%	0.5–3%	0.018–0.02	0.005–0.034
ρ_4 837 ± 107 nm	···	3.5–14%	0.007–0.009	0.003–0.023
ρ_5 1692 ± 178 nm	···	5–16%	0.000–0.001	0.001–0.007
ρ_7 2190 ± 215 nm	···	2.5–13%	···	0.001–0.004
NDVI (bare soil) ρ_3 = 0.19, ρ_4 = 0.22	0.015–0.041	0.015–0.06	0.03	0.006–0.032

The proportional effect (transmission) is given as percentage (%) of increase or reduction of the signal. All other effects as well as the effect on the NDVI are given in absolute units.

where ρ_{R+A} is the intrinsic atmospheric reflectance due to Rayleigh and aerosol scattering, $T_{R+A}(\mu_s)$ (respectively $T_{R+A}(\mu_v)$) is the total downward (respectively upward) atmospheric transmission, S_{R+A} is the spherical albedo of the atmosphere, μ_s (respectively μ_v) is the cosine of the Sun (respectively view) zenith angle.

When taking into account the adjacency effect, the signal at the top of the atmosphere can be rewritten by decoupling the photons coming directly from the target ($e^{-\tau/\mu_v}$) from those coming from areas adjacent to the target and then scattered to the sensor ($t_d(\mu_v)$):

$$\rho_{\text{TOA}} = \rho_{R+A} + \frac{\rho_s T_{R+A}(\mu_s) e^{-\tau/\mu_v} + \langle \rho_s \rangle T_{R+A}(\mu_s) t_d(\mu_v)}{1 - \langle \rho_s \rangle S_{R+A}}. \quad (2)$$

τ is the atmospheric optical depth, $t_d(\mu_v)$ is the diffuse upward transmission, ρ_s is the pixel reflectance, and $\langle \rho_s \rangle$ is the contribution of the pixel background to the top of the atmosphere signal that is computed as

$$\langle \rho_s \rangle = \int_{-\infty}^{+\infty} \int_{-\infty}^{+\infty} f(r(x, y)) \rho(x, y)\, dx\, dy, \quad (3)$$

where x, y denotes the coordinate to a local reference centered on the target, and $f(r)$ is the atmospheric point spread function.

We can see that if we consider that $1/(1 - \langle \rho_s \rangle S_{R+A}) \cong 1/(1 - \rho_s^u S_{R+A})$, then ρ_s and ρ_s^u (from (1)) are related through the following equation:

$$\rho_s^u = \rho_s \frac{e^{-\tau/\mu_v}}{T_{R+A}(\mu_v)} + \langle \rho_s \rangle \frac{t_d(\mu_v)}{T_{R+A}(\mu_v)}. \quad (4)$$

Therefore we can correct the reflectance, obtained from (1), ρ_s^u for the adjacency effect using

$$\rho_s = \frac{\rho_s^u T_{R+A}(\mu_v) - \langle \rho_s \rangle t_d(\mu_v)}{e^{-\tau/\mu_v}}. \quad (5)$$

In practice, $\langle \rho_s \rangle$ is computed from a subzone of $(2n + 1) \times (2n + 1)$ pixels of the original image centered on the pixel to be corrected using ($\rho_s^u(i, j)$ is used instead of $\rho_s(i, j)$ since the latter is not available; the error introduced can be reduced by using successive iterations but is small [*Putsay*, 1992])

$$\langle \rho_s \rangle = \sum_{j=-n}^{n} \sum_{i=-n}^{n} f(r(i, j)) \rho_s^u(i, j), \quad (6)$$

with $r(i, j)$ representing the distance between the pixels (i, j) and the center of the zone.

As part of a NASA-funded collaboration with the National Science Foundation (NSF) Long-Term Ecological Research (LTER) site network on atmospheric correction validation, we applied the technique previously presented for correction of the atmospheric point spread function. This technique was applied to the Landsat TM data (30 m resolution) up to a distance of 20 pixels around the viewed pixel. Two optimizations were necessary to arrive at an acceptable processing time (about twice the amount of time of a simple correction). First, we generated (over the range of expected values) a look-up table of the product $f(r(i, j))\rho_s^u(i, j)$. By using the look-up table, we do not perform any multiplication to compute (6) and reduce the processing time significantly. Secondly, the computation for the pixel of coordinate $(k, l)\langle \rho_s(k, l) \rangle$ was computed from its neighbor at coordinate $(k, l - 1)\langle \rho_s(k, l - 1) \rangle$, the advantage here being that the atmospheric point spread function is rather smooth and that the difference matrix between two adjacent pixels contains many zeroes. By sorting the difference matrix values and eliminating the zero elements, we were further able to reduce the number of operations to be performed by roughly a factor of 10. Figure 2 illustrates the results of the adjacency effect correction for TM band 1. The scene was acquired over a coastal area in the eastern United States. On the left side is the corrected image; on the right side is the original digital count image. The top part represents the full subset (1000 × 1000 pixels); the bottom part represents an enlargement of a part of the scene. The corrected scene appears to show more contrast than the uncorrected scene due to the correction of atmospheric reflectance and transmission terms. The enlarged detail shows the impact and correction of the adjacency; the small dark area in the original scene was previously less visible because it was surrounded by brighter pixels.

For MODIS the surface adjacency effect correction will be made up to a distance of 10 pixels using the same technique developed for the TM. Because the atmospheric point spread function varies with the view angle as illustrated by Figure 3, we will use precomputed tables as a function of view angle.

2.2. BRDF Atmosphere Coupling Correction

If the surface is not Lambertian, the result of the correction using (1) is inexact due to the coupling between the surface BRDF and the atmosphere BRDF [*Lee and Kaufman*, 1986] which the equation does not take into account. For example, Figure 4 shows the difference between the true ground reflectance (ρ_s), and the reflectance computed without coupling (ρ_s^{da}) can reach 0.02 for off-nadir views.

An approach to model/correct this effect stems from the work of *Tanré et al.* [1983]. The contribution of the target to the signal at the top of the atmosphere is decomposed as the sum of four terms: (1) the photons directly transmitted from the Sun to the target and directly reflected back to the sensor, (2) the photons scattered by the atmosphere then reflected by the target and directly transmitted to the sensor, (3) the photons directly transmitted to the target but scattered by the atmosphere on their way to the sensor, and finally (4) the photons having at least two interactions with the atmosphere and one with the target. The equation is written as [*Vermote et al.*, 1997]:

$$\rho_{\text{TOA}}(\mu_s, \mu_v, \phi_s - \phi_v) = \rho_{R+A}$$

$$\overbrace{\qquad\qquad}^{(1)}$$

$$+ e^{-\tau/\mu_v} e^{-\tau/\mu_s} \rho_s(\mu_s, \mu_v, \phi_s - \phi_v)$$

$$\overbrace{\qquad}^{(2)} \quad \overbrace{\qquad}^{(3)}$$

$$+ e^{-\tau/\mu_v} t_d(\mu_s)\bar{\rho} + e^{-\tau/\mu_s} t_d(\mu_v)\overline{\rho'}$$

$$\overbrace{\qquad\qquad}^{(4)}$$

$$+ t_d(\mu_s) t_d(\mu_v) \bar{\rho} + \frac{T_{R+A}(\mu_s) T_{R+A}(\mu_v) S(\bar{\rho})^2}{1 - S\bar{\rho}}, \quad (7)$$

with ϕ_s (resp. ϕ_v) the Sun (resp. view) azimuth angle, and

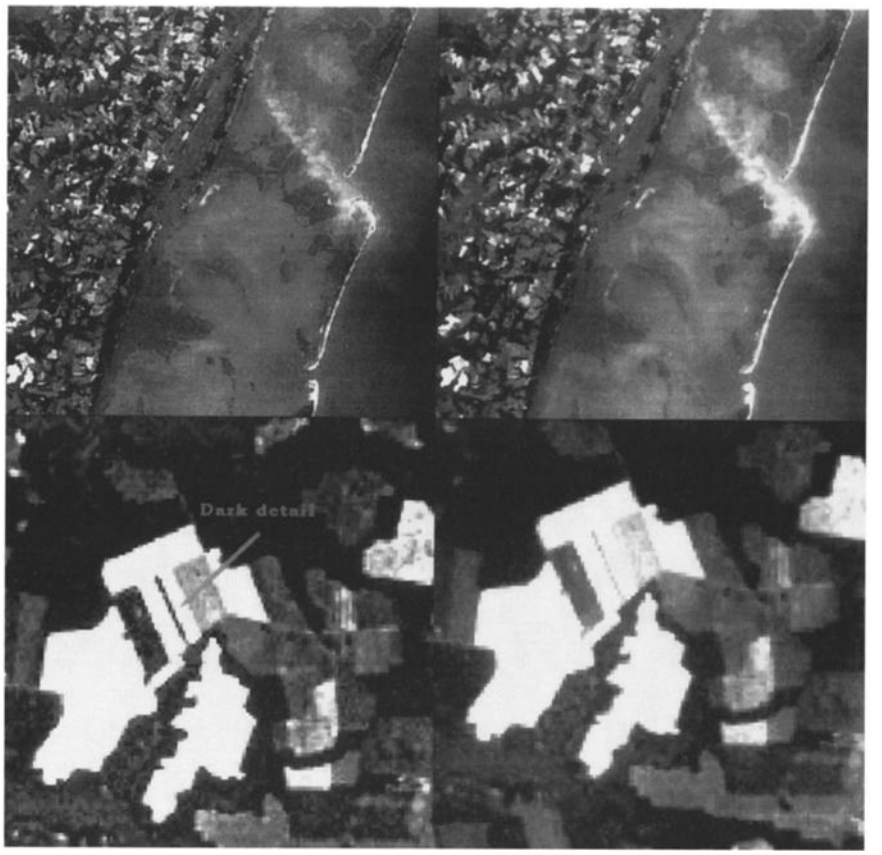

Figure 2. Comparison of Thematic Mapper (TM) band 1 data corrected for atmosphere (left side) to uncorrected counts (right side). The correction includes adjacency effect correction.

$$\bar{\rho}(\mu_s, \mu_v, \phi) = \frac{\int_0^{2\pi}\int_0^1 \mu L^{\downarrow}_{R+A}(\tau_A, \tau_R, \mu_s, \mu, \phi')\rho_s(\mu, \mu_v, \phi' - \phi)\, d\mu\, d\phi'}{\int_0^{2\pi}\int_0^1 \mu L^{\downarrow}_{R+A}(\tau_A, \tau_R, \mu_s, \mu, \phi')\, d\mu\, d\phi'}, \tag{8a}$$

where τ_R (resp. τ_A) are the Rayleigh (resp. aerosol) optical depth, and

$$\overline{\rho'}(\mu_s, \mu_v, \phi) = \bar{\rho}(\mu_v, \mu_s, \phi), \tag{8b}$$

$$\bar{\bar{\rho}} = \overline{\overline{\rho'}(\mu_s, \mu_v, \phi)}, \tag{8c}$$

$$\bar{\bar{\rho}} \cong \frac{\int_0^1\int_0^1\int_0^{2\pi}\int_0^1 \rho_s(\mu, \mu', \phi)\mu\mu'\, d\mu'\, d\phi\, d\mu}{\int_0^1\int_0^1\int_0^{2\pi}\int_0^1 \mu\mu'\, d\mu'\, d\phi\, d\mu}. \tag{8d}$$

In our approach, we use the ratio between the estimated BRDF (ρ_s^m) coupled with the atmosphere and the actual surface BRDF (ρ_s) to correct the measured values; that is,

$$\rho_{\mathrm{TOA}}(\mu_s, \mu_v, \phi) = \rho_{R+A} + e^{-\tau/\mu_v}e^{-\tau/\mu_s}\rho_s(\mu_s, \mu_v, \phi) + \rho_s(\mu_s, \mu_v, \phi)$$
$$\cdot\left[e^{-\tau/\mu_v}t_d(\mu_s)\overline{\rho^*} + e^{-\tau/\mu_s}t_d(\mu_v)\overline{\rho'^*} + t_d(\mu_s)t_d(\mu_v)\overline{\bar{\rho}^*} + \rho_s(\mu_s, \mu_v, \phi)\frac{T^{\downarrow}_{R+A}(\mu_s)T^{\uparrow}_{R+A}(\mu_v)S(\overline{\rho^*})^2}{1 - S\bar{\bar{\rho}}}\right], \tag{9a}$$

with

$$\overline{\rho^*}(\mu_s, \mu_v, \phi) = \frac{\overline{\rho^m}(\mu_s, \mu_v, \phi)}{\rho_s^m(\mu_s, \mu_v, \phi)}, \tag{9b}$$

$$\overline{\rho'^*}(\mu_s, \mu_v, \phi) = \overline{\rho^*}(\mu_v, \mu_s, \phi), \tag{9c}$$

$$\overline{\bar{\rho}^*}(\mu_s, \mu_v, \phi) = \frac{\overline{\bar{\rho}^m}(\mu_s, \mu_v, \phi)}{\rho_s^m(\mu_s, \mu_v, \phi)}. \tag{9d}$$

The solving of (9a) for ρ_s is done by solving a second-order equation that only has one positive solution. The rationale behind this approach is that only the "shape" of the BRDF influences the correction process and not the actual "magnitude" of the estimated BRDF. This approach gives more weight to the actual observation than to the estimated BRDF used. Both the surface BRDF (ρ_s^m) and the atmosphere coupled BRDF terms ($\overline{\rho^m}$, $\overline{\bar{\rho}^m}$) can be precomputed and stored in tables.

We are currently investigating two alternative approaches for obtaining modeled BRDF inputs. One approach is to use the linear BRDF model parameters derived from the previous 16 day period, generated as part of the MODIS BRDF product [*Strahler et al.*, 1995]. The other approach relies on the BRDF

associated with land cover categories used in the MODIS LAI/FPAR product [*Running et al.*, 1994] and simulated using a three-dimensional canopy model [*Myneni et al.*, 1992]. In the latter case, BRDF and coupling terms are stored in tables as a function of Sun-view geometry, atmospheric optical depth, biome type, and LAI. The biome is determined by the land cover map, and the LAI is selected by minimizing the difference between the spectral dependence of observed and modeled reflectance in MODIS bands 1, 2, 3, and 4. The advantage in using the first approach is that the BRDF shape is more linked to actual observations; the advantage in the second case is that the coupling correction can be estimated in real time. A comparison of the relative merits of these approaches will be made in the near future.

3. Implementation for Global Processing

3.1. Processing Scheme

As currently developed, the atmospheric correction process ingests the MODIS-calibrated radiances and estimates the surface reflectances. In addition to the estimates of the surface reflectance the data product contains the following quality assurance (QA) information for each pixel: (1) integrity of the surface reflectance estimate; (2) successful completion of the correction scheme; (3) presence of cloud (clear, cloudy, mixed, shadow); (4) presence of cirrus cloud (no cirrus, low, average, high); (5) source of aerosol information: MODIS aerosol, climatology; (6) presence of aerosol (low, average, high); (7) source of water vapor information: MODIS water vapor, climatology; (8) source of ozone information: MODIS ozone, climatology; (9) whether the datum is from land or water.

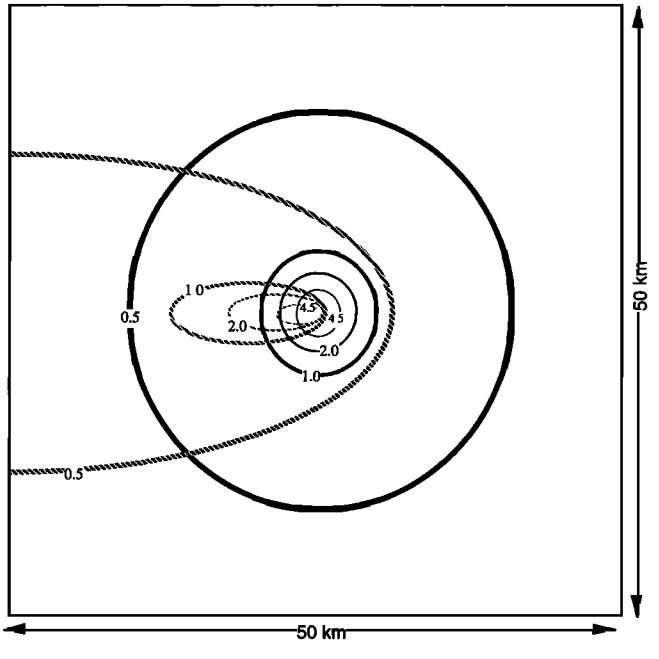

Figure 3. Isolines of the pixel background contribution to the signal at the top of the atmosphere for a pure molecular case. The energy source is 10^4 W and each pixel is considered to have a Lambertian reflectance of 1. The contribution of the background is presented as the number of watts coming from each cell (201 cells × 201 cells). The plain lines are for nadir viewing; the broken lines are for a view angle of 70° [from *Vermote et al.*, 1997].

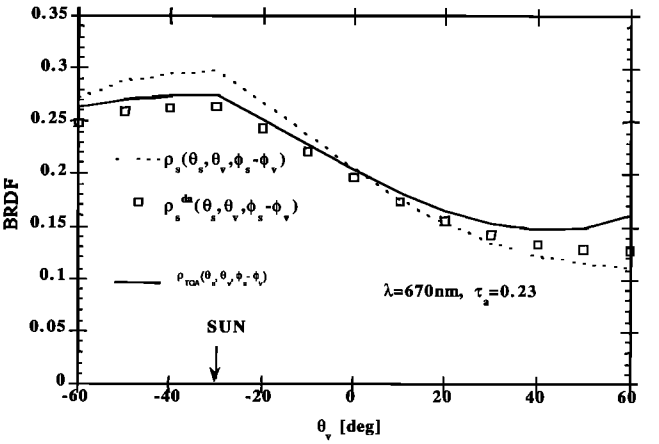

Figure 4. Illustration of the atmosphere-bidirectional distribution function (BRDF) coupling effect correction. The surface reflectance ρ_s is computed by the Hapke model (the parameters are inverted from surface reflectance directional data taken over a plowed field by *Kimes et al.* [1986]) and corresponds to the interrupted line. The plain line corresponds to the top of the atmosphere signal, ρ_{TOA}, at 670 nm, assuming average atmospheric turbidity. The surface reflectances retrieved using the Lambertian hypothesis or equation (1), ρ_s^{da}, are represented by the open squares.

The current version of the software is the first that reads MODIS synthetic data (A. Fleig and K. Yang, personal communication, 1995) and writes MODIS products using the HDF (hierarchical data format) structure. In this code we were able to successfully implement the correction for the atmospheric point spread function and the coupled atmosphere surface BRDF. Each of these corrections can be selectively activated. Figure 5 gives a global overview of the current software functionality, data volumes, and central processing unit (CPU) requirements.

3.2. Developing Aerosol Climatology

Because the aerosol product being generated by the MODIS atmosphere group is a critical input to the atmospheric correction scheme [*Tanré et al.*, 1992], validation and prototyping of the aerosol product and correction deserve special cooperation between the atmosphere and the land groups. Software development activities are currently focused on the aerosol climatology. We need to understand on a global basis the impact of aerosols. We have therefore based our approach on the advanced very high resolution radiometer (AVHRR) data. This activity is important for MODIS for three different reasons: (1) it provides the default input to the atmospheric correction algorithm should the MODIS aerosol product be unavailable, (2) it can contribute to the validation of the aerosol algorithm for MODIS, and (3) it validates the aerosol atmospheric correction process for AVHRR data. We have currently developed a prototype approach to generate this climatology. Plate 1 shows over the tropical belt area a composite of the aerosol optical depth during first week of September 1993. Smoke from biomass burning (Brazil and South Africa) and dust from arid area (Red Sea and East Africa) aerosol can clearly be observed. An important source of perturbation for vegetation monitoring is the stratospheric aerosols after a significant volcanic eruption. The stratospheric aerosols have long lifetime and therefore could be eliminated in monthly compos-

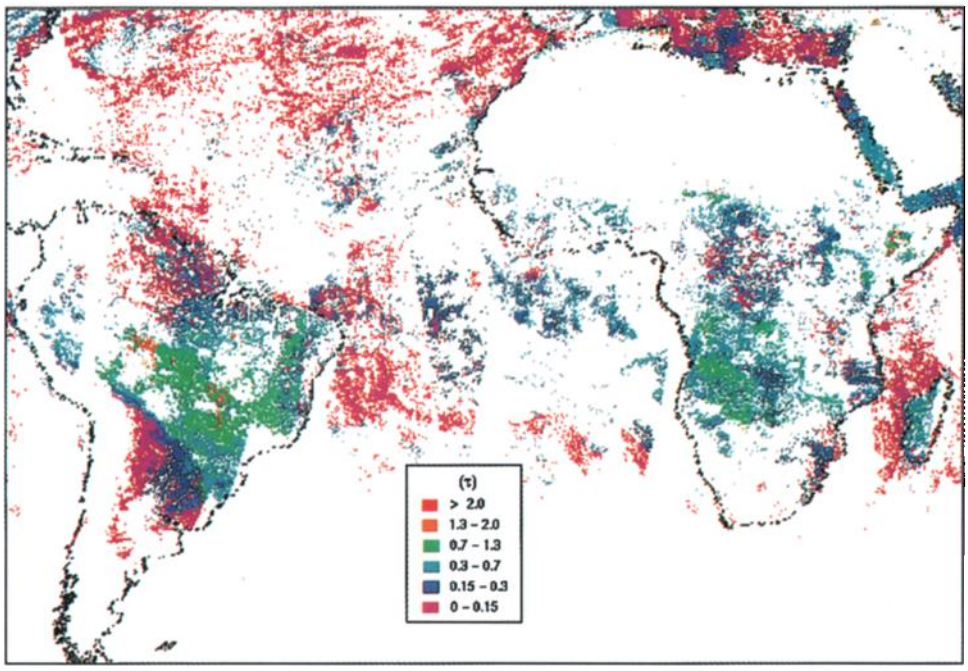

Plate 1. Maximum aerosol optical thickness at 550 nm during the week September 3–9, 1993, derived from NOAA AVHRR global area coverage (GAC) data.

ites as well as tropospheric aerosols. Since 1981, two important volcanic eruptions affected global vegetation monitoring, El Chichon and Mount Pinatubo, as illustrated by Plate 2.

4. Validation Plan

Validation activities can be divided into prelaunch validation of the algorithm and postlaunch validation of the product. The MODIS surface reflectance product validation will use a combination of ground-based measurements, airborne measurements, comparison with other sensor data, and image analysis.

4.1. Methodology

Validation of the reflectance product will be undertaken for selected global test sites as part of the proposed EOS Test Site Program, where a suite of measurements for atmosphere, surface reflectance, and other surface parameters such as LAI, FPAR, and net primary production (NPP) will be collected

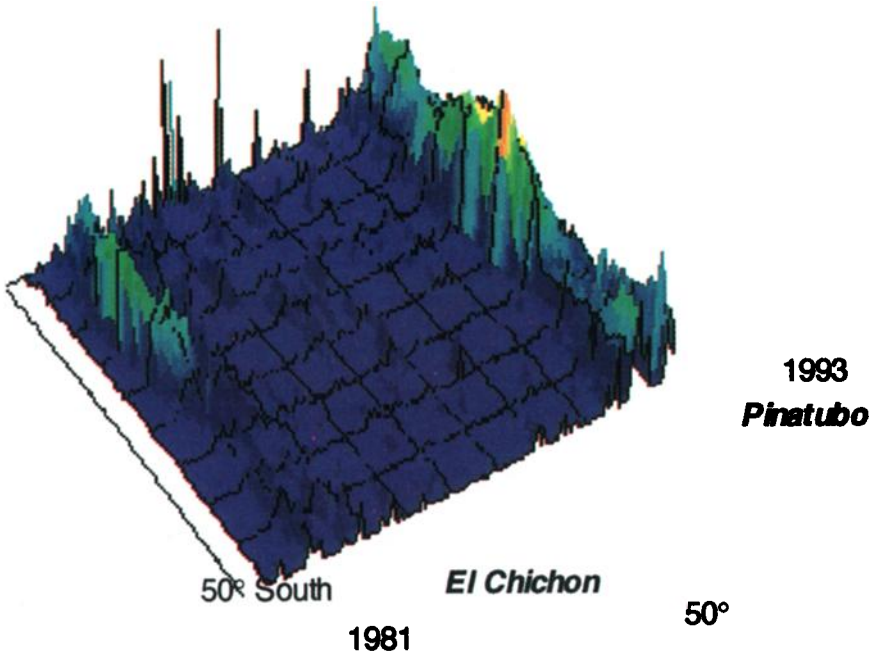

Plate 2. Monthly average of the stratospheric aerosol optical depth deduced from the advanced very high resolution radiometer (AVHRR) data showing major eruptions of El Chichon (1982) and Pinatubo (1991).

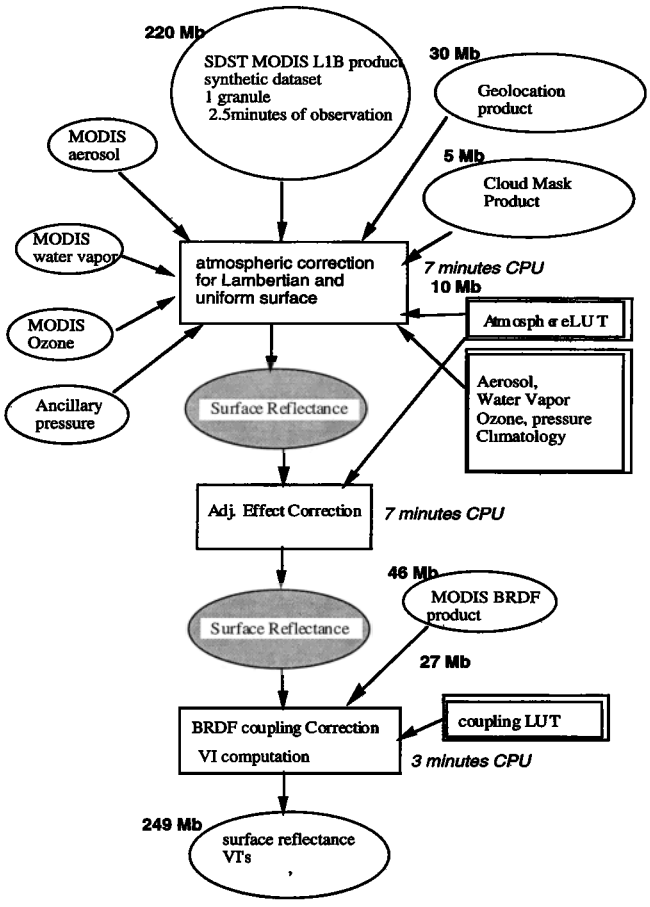

Figure 5. Current moderate resolution imaging spectroradiometer (MODIS) atmospheric correction processing thread flowchart.

[*Running et al.*, 1994]. These measurements will be made at different temporal frequencies as appropriate for the parameters. It is important to consider several factors when evaluating the atmospheric correction, for example under changing Sun/sensor geometry, atmospheric state, and surface state. As part of the surface reflectance validation, we propose to conduct a maximum of four campaigns a year corresponding to seasonal changes in surface state and Sun geometry. For each of these campaigns, we will collect surface reflectance and atmospheric state data with simultaneous satellite coverage. Both clear and turbid atmospheres are desirable for each campaign as well as data gathered at four or five different viewing geometries (nadir, backscattering, forward scattering). Dark and bright surface measurements will be collected for each campaign, given that the success of the correction for a dark surface depends mainly on the correct estimate of the intrinsic atmospheric reflectance, whereas for a bright surface it depends on the correct estimate of the transmittance. Critical to this plan is the continuation and expansion of AERONET [*Holben et al.*, 1997], which provides data on optical depth and aerosol as well as size distribution on a continuous basis (see Figure 6 for current locations). The total number of sites needed for validation is related to two requirements: (1) the expected variability of atmospheric conditions; (2) spectral signatures and anisotropic properties of the different land covers. We expect to need approximately 2–3 sites in the polar environment (polar regions), 7–8 sites in the boreal environment (Canada, Greenland, Norway-Sweden, Russia), 5–6 sites in North America, 5–6 sites in western Europe, and 5–6 sites in eastern Europe. More sites will be needed in the tropical areas because of the importance of aerosol variability and transport and the rapid temporal change in land cover (e.g., at desert boundaries). There are currently 18 Sun photometers installed in the tropics that mainly cover Brazil (12) with some in Africa (6). Ideally, we need at least 12 more in Africa and 12 more for the rest of the tropics to cover Asia. The southern hemisphere, including South America, southern Africa, and Australia, will need at least 7–8 sites with 2–3 sites in the southern polar region. On the basis of this allocation the total number of sites is between 69 and 74. Further details on validation methods and sites are available on the internet through the EOS Validation Office MODIS summary charts.

Limiting errors in surface reflectance to less than 0.005 rms for clear conditions and 0.01 rms for turbid conditions (5 km visibility) will be considered a success for the atmospheric correction. To meet this goal, MODIS radiometric calibration (relative to the Sun) should have at least 2% accuracy. Because finite cloud fields modify the downward radiation field, we expect a decrease in the performance of the algorithm under these conditions. Cloud situations should be included in the validation data collection to assess the change in algorithm performance.

4.2. Prototyping Activities

Two tasks need to be addressed when generating/validating a global "product" before launch. The first task is to validate how the algorithm performs with a similar data set ("science validation"). For this product the approach will be to continue and expand on the LTER atmospheric correction project. The LTER project is particularly relevant as the TM data used in this study includes several of the spectral bands planned for MODIS. AERONET Sun photometer data are collected at these sites simultaneously with the satellite data. Figure 7a illustrates the validation of the aerosol retrieval algorithm with TM data. In this case, optical depth deduced from band 1 and 3 "dark targets" reflectances are compared to Sun photometer measurements. The "dark targets" are selected by using the pixels whose reflectance at 2.14 μm are between 0.015 and 0.05 and whose normalized difference vegetation index (NDVI) is greater than zero (to eliminate water bodies). The average "dark target" reflectance in band 1 is computed on a 50 km × 50 km area around the Sun photometer, and the surface reflectance in band 1 is assumed to be one third of the reflec-

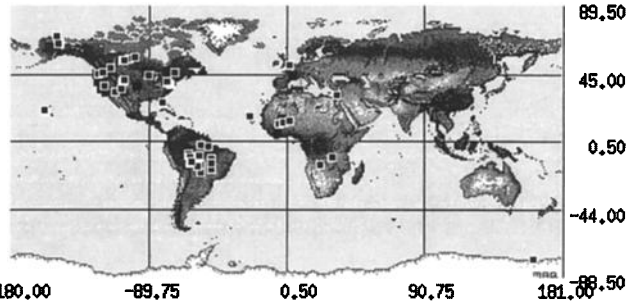

Figure 6. Sun photometer network locations (source, B. N. Holben, NASA GSFC). The vertical axis is the latitude in degree (south is negative, north is positive), the horizontal axis is the longitude in degree (west is negative, east is positive).

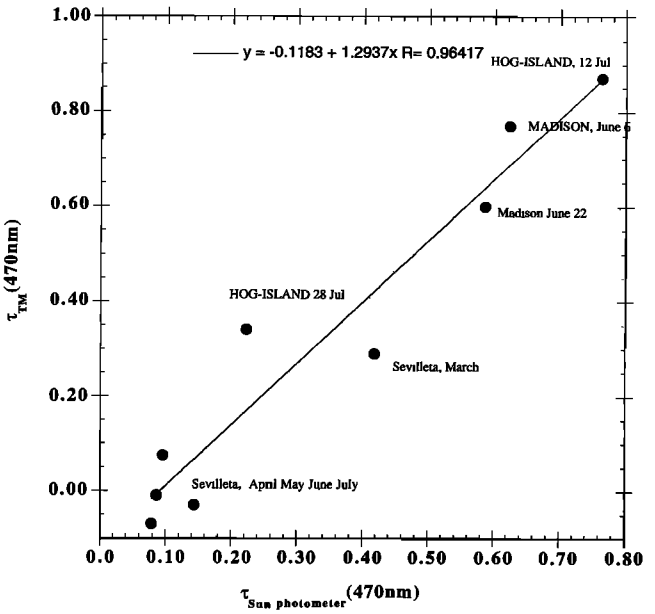

Figure 7a. Retrieval of optical depth in TM band 1 using the "dark targets" approach (band 7 at 2.14 μm is used for "dark targets" detection) compared with Sun photometer data.

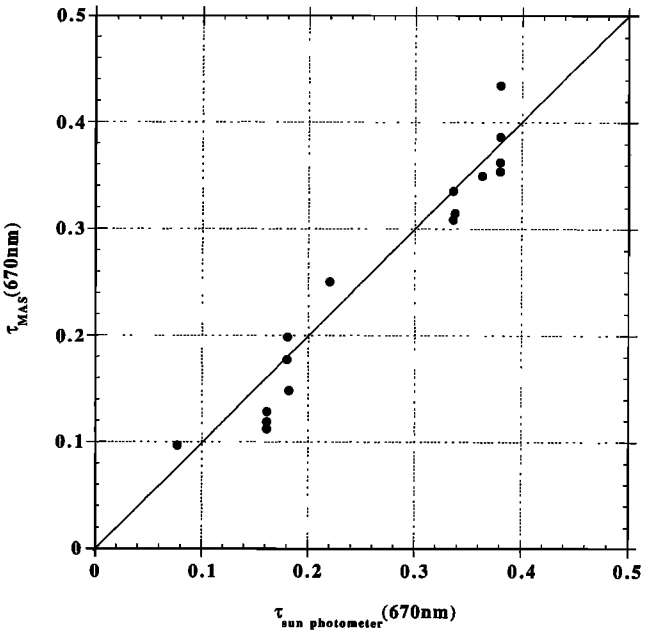

Figure 8a. Retrieval of aerosol optical depth using the dark target technique with the 2.14 μm from MODIS airborne simulator (MAS) data during the SCAR A experiment [*Roger et al.*, 1994].

tance observed at 2.14 μm. Figure 7a shows comparisons of the derived optical depth using a continental aerosol model versus the measured optical depth. Despite some very low and slightly negative values observed for the Sevilleta, New Mexico, site that may be due to the topography of the area, the agreement is encouraging. More encouraging is the comparison shown in Figure 7b. These histograms of band 1 reflectance for the Hog Island, Virginia, LTER site for clear and hazy days show that the atmospheric correction process clearly removed the artifacts introduced by the aerosol temporal variability.

A further approach to validation is to use high-altitude airborne data from MAS as we did during the Sulfate Cloud Aerosol Reflectance-Atlantic (SCAR A) experiment [*Roger et al.*, 1994]. Using the MODIS airborne simulator (MAS), we tested the 2.14 μm approach for detecting "dark targets" over six test sites using the same test as described for TM. In Figure 8a, aerosol retrieval was performed for "dark targets" using the 0.67 μm MAS band (a reflectance of 0.015 was assumed for dark targets at 0.67 μm) and a continental aerosol model. The

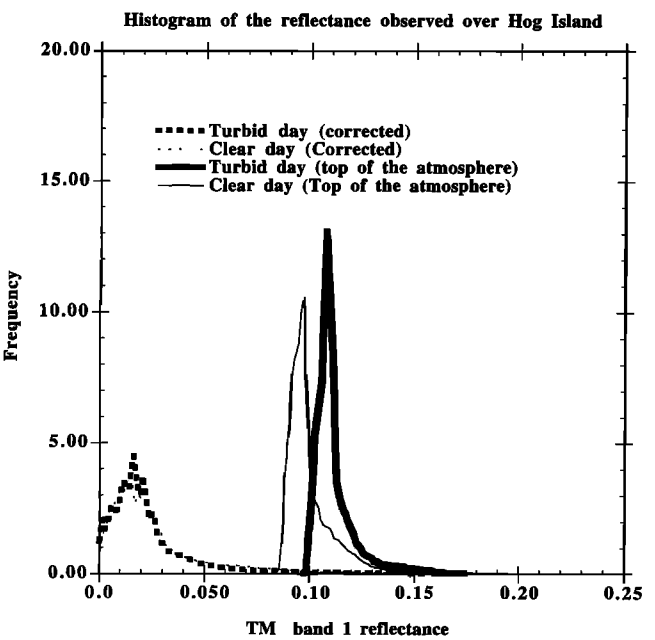

Figure 7b. Test of the result of the atmospheric correction procedure (including aerosol retrieval and atmospheric point spread function correction) for a 1000 × 1000 TM pixels area of the Hog Island site for the clear and hazy day.

Table 2. Results of the Inversion of Top of the Atmosphere and Top of the Canopy Using SCAR A MAS Data Set

	Leaf Area Index	Leaf Reflectance	Leaf Angle Distribution	rms
Green band top of atmosphere reflectance	0.4	0.010	planophile	0.26×10^{-3}
Green band top of canopy reflectance	9.2	0.105	erectophile	0.44×10^{-4}
Red band top of atmosphere reflectance	1.2	0.150	erectophile	0.135×10^{-4}
Red band top of canopy reflectance	2.7	0.070	erectophile	0.137×10^{-4}
Green band expected values	>3	0.05–0.25	erectophile	
Red band expected values	>3	0.03–0.16	erectophile	

SCAR A MAS, Sulfate Cloud Aerosol Reflectance-Atlantic MODIS airborne simulator.

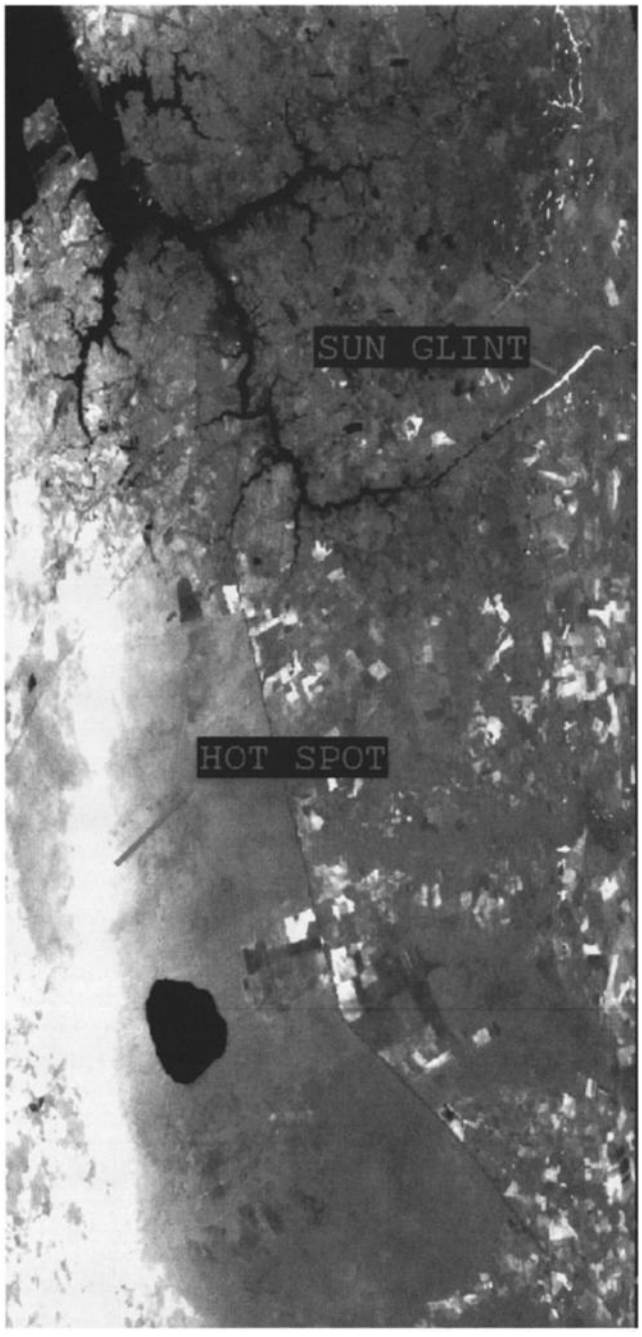

Figure 8b. Grey level image of the MAS scene (0.87 μm) used in the BRDF inversion (Figure 8c and 8d). Annotations on the images point to the forest hot spot and water sun glint features.

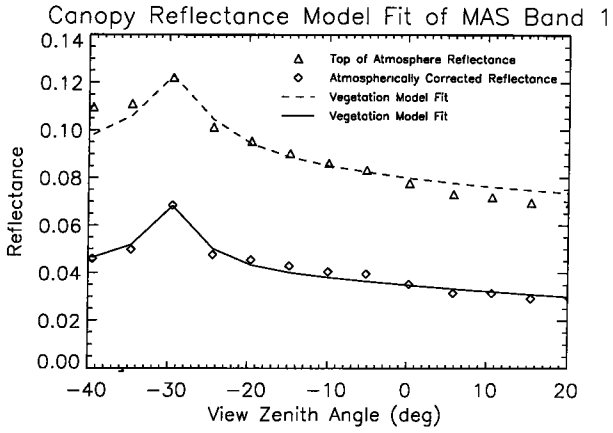

Figure 8c. Fits of MAS principal plane data using *Myneni et al.* model [1992] using corrected (plain lines, diamonds) and top of the atmosphere (dashed line, triangles) for the green band (0.55 μm).

optical depth measurements from AERONET compared well to MAS retrievals. In that case, the effect of the aerosol model is more sensitive than for TM as the scattering angle of the different observations varies (from 110° to 150°). For SCAR A MAS data, strong directional surface reflectance effects could be observed over forest with a particularly sharp hot spot phenomenon (Figure 8b). We were able to fit the MAS data using a physically based model [*Myneni et al.*, 1992]. The results are shown in Figures 8c and 8d. In the green band, where atmospheric scattering is larger, the atmospheric correction definitely improves the fit of the data both in backscatter and in forward scattering directions (Figure 8c). In the red band, both corrected and uncorrected data are fit well. The difference is important for the retrieved surface parameters (Table 2), whether the top of the atmosphere reflectance or the surface estimated reflectance or top of the canopy is used. The parameters derived from top of the canopy reflectance values are closer to the expected values than the ones derived from top of the atmosphere reflectance for this forest case. The LAI is higher in the green band than in the red band, but it is quite difficult to retrieve LAI values above 3 because of the saturation of the signal, and therefore LAI errors are common with dense canopies.

The second task concerns validating the global applicability and robustness of the algorithm. We can test the algorithm data flow by using the MODIS synthetic data set being developed by the MODIS science data support team (SDST), although the science cannot be thoroughly tested using these data because we are comparing one model output with another. The global processing issue has to be addressed with real data. We plan to start to test the global applicability of the MODIS algorithm using AVHRR time series data. Collaboration will be developed with the NASA EOS AVHRR Path-

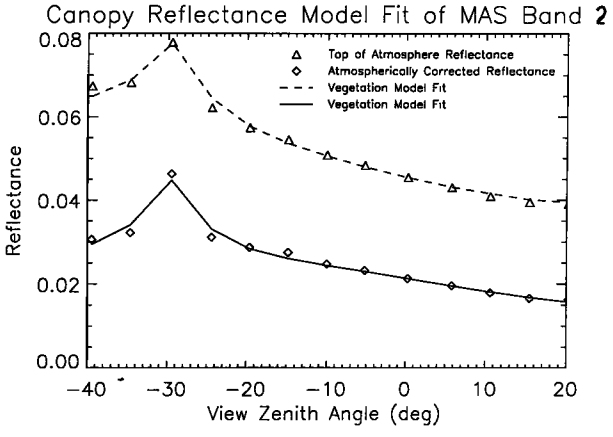

Figure 8d. Fits of MAS principal plane data using *Myneni et al.* model [1992] using corrected (solid lines, diamonds) and top of the atmosphere (dashed line, triangles) for the red band (0.67 μm).

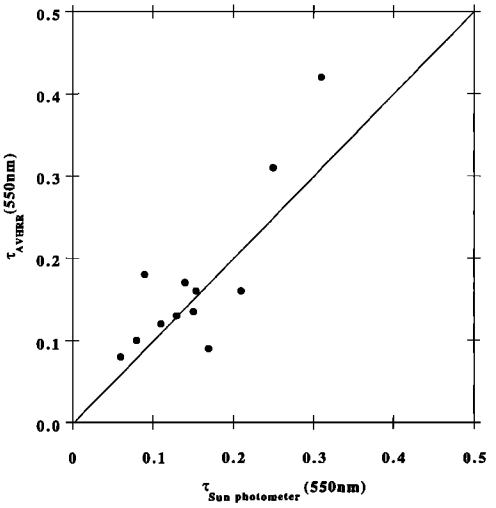

Figure 9a. Comparison of retrieved optical depth using AVHRR data and the dark target approach and measured optical depth from the Sun photometer network in August 1993 over eastern United States.

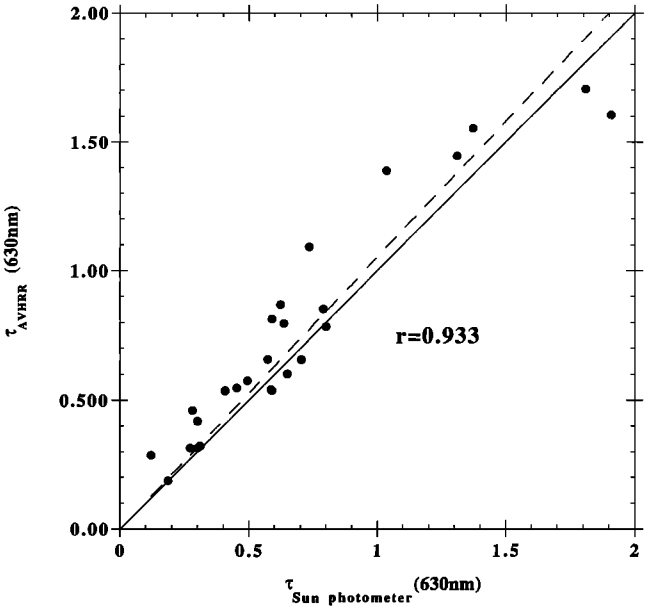

Figure 9c. Same as Figure 9b but in 1993.

finder 2 Project, whose goal is to improve on the current AVHRR Pathfinder by designing and testing global processing of AVHRR 1 km and 4 km land data as a pathfinder for MODIS. This MODIS prototyping using the AVHRR will include operational correction for Rayleigh, ozone, water vapor, and stratospheric aerosol and will investigate the possibility of correcting for tropospheric aerosols. These corrections will be conducted at a global scale over a range of actual atmospheric and surface conditions. As an example of the tropospheric aerosol correction effort, we obtained some very encouraging results by using AVHRR data to retrieve aerosol at specific land sites. In these cases the 3.75 μm reflectance [*Roger and Vermote*, 1996] was used in lieu of the 2.14 μm to detect dark targets using a threshold of 0.03. Figures 9a and 9b show the results of AVHRR optical depth retrieval during the SCAR A campaigns and the 1992 AERONET Brazil data set. In both cases a continental aerosol model was used. Figure 9c shows the results of AVHRR retrieval over Brazil using AERONET 1993 August–September data and a smoke model derived from AERONET aerosol size distribution.

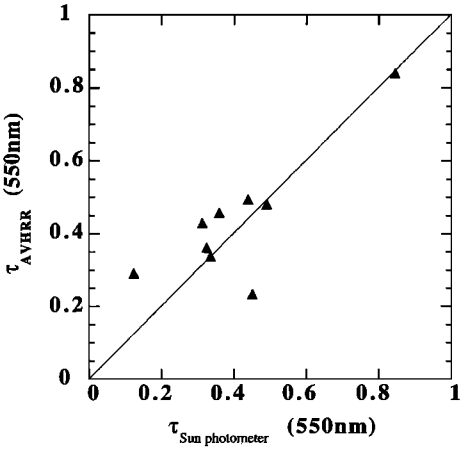

Figure 9b. Same as Figure 9a but in 1992 over Brazil.

5. Conclusion

The present paper describes the approach adopted for computing the surface reflectance in MODIS visible to middle-infrared land bands. The processing of the top of the atmosphere signal to obtain surface reflectance is not perfect but does incorporate state of the art techniques. We are currently working on operational prototypes using existing data sources for the prelaunch algorithm and product validation phase. In addition to AVHRR and Landsat TM we are planning to use test data sets from the polarization and directionality of the Earth's reflectances (POLDER) instrument and the sea-viewing wide field-of-view sensor (SeaWiFS) instrument corresponding to our selected test sites. Postlaunch, the advanced spaceborne thermal emission and reflection radiometer (ASTER), the multi-angle imaging spectroradiometer (MISR), and the Landsat 7 Enhanced Thematic Mapper Plus (ETM+) data will be used during validation campaigns. Moreover, the limited number of test sites will make it practical to systematically cross-compare different sensors. MISR will definitely improve our knowledge of BRDF and ASTER and Landsat 7/ETM+ should enable us to extrapolate local ground-based measurements to the MODIS pixels.

References

Holben, B. N., et al., Automatic Sun and sky scanning radiometer system for Network Aerosol Monitoring, *Remote Sens. Environ.*, in press, 1997.

Kaufman, Y. J., Solution of the equation of radiative transfer for remote sensing over two-dimensional surface reflectivity, *J. Geophys. Res.*, *20*, 4137–4147, 1982.

Kaufman, Y. J., D. Tanré, L. Remer, E. F. Vermote, A. Chu, and B. N. Holben, Operational remote sensing of tropospheric aerosol over land from EOS moderate resolution imaging spectroradiometer, *J. Geophys. Res.*, this issue.

Kimes, D. S., W. W. Newcomb, R. F. Nelson, and J. B. Schutt, Directional reflectance distributions of a hardwood and pine forest canopy, *IEEE Trans. Geosci. Remote Sens.*, *GE-24*(2), 281–293, 1986.

Lee, T. Y., and Y. J. Kaufman, Non-Lambertian effects on remote sensing of surface reflectance and vegetation index, *IEEE Trans. Geosci. Remote Sens.*, *GE-24*, 699–708, 1986.

Mekler, Y., and Y. J. Kaufman, The effect of Earth's atmosphere on contrast reduction for a nonuniform surface albedo and two-halves field, *J. Geophys. Res.*, *85*, 4067–4083, 1980.

Myneni, R. B., G. Asrar, and F. G. Hall, A three dimensional radiative transfer model for optical remote sensing of vegetated land surfaces, *Remote Sens. Environ.*, *41*, 85–103, 1992.

Putsay, M., A simple atmospheric correction method for the short wave satellite image, *Int. J. Remote Sens.*, *13*(8), 1549–1558, 1992.

Roger, J. C., and E. F. Vermote, Computation and use of the reflectivity at 3.75 μm from AVHRR thermal channels, *Remote Sens. Rev.*, in press, 1996.

Roger, J. C., E. F. Vermote, and N. El Saleous, Atmospheric correction of MAS data during SCAR-A experiment, in *Atmospheric Sensing and Modeling, SPIE Proc.*, *2311*, 83–89, 1994.

Running, S. W., et al., Terrestrial remote sensing science and algorithms planned for EOS/MODIS, *Int. J. Remote Sens.*, *15*(17), 3587–3620, 1994.

Strahler, A. H., M. J. Barnsley, R. d'Entremont, B. Hu, P. Lewis, X. Li, J. Muller, C. B. Schaaf, W. Wanner, and B. Zhang, MODIS BRDF/albedo product version 3.2, Algorithm technical background document, *NASA EOS-MODIS Doc. Update*, 65 pp., 1995.

Tanré, D., M. Herman, and P. Y. Deschamps, Influence of the background contribution upon space measurements of ground reflectance, *Appl. Opt.*, *20*, 3673–3684, 1981.

Tanré, D., M. Herman, and P. Y. Deschamps, Influence of the atmosphere on space measurements of directional properties, *Appl. Opt.*, *21*, 733–741, 1983.

Tanré, D., B. N. Holben, and Y. J. Kaufman, Atmospheric Correction algorithm for NOAA-AVHRR products: Theory and application, *IEEE Trans. Geosci. Remote Sens.*, *30*(2), 231–248, 1992.

Vermote, E., L. A. Remer, C. O. Justice, Y. J. Kaufman, and D. Tanré, Atmospheric correction algorithm: Spectral reflectances (MOD09), version 2.0, Algorithm technical background document, *NASA EOS-ID 2015 Doc.*, 42 pp., 1995.

Vermote, E. F., D. Tanre, J. L. Deuze, M. Herman, and J. J. Morcrette, Second simulation of the satellite signal in the solar spectrum: An overview, *IEEE Trans. Geosci. Remote Sens.*, in press, 1997.

C. O. Justice, J. L. Privette, N. El Saleous, and E. F. Vermote, NASA GSFC Code 923, Greenbelt, MD 20771. (e-mail: eric@kratmos.gsfc.nasa.gov)

Y. J. Kaufman and J. C. Remer, NASA Goddard Space Flight Center, Code 913, Greenbelt, MD 20771.

J. C. Roger, Laboratoire de Physique Appliquée aux Milieux Oceaniques Côtiers, Station Marine-Université du Littoral, France.

D. Tanre, Laboratoire d'Optique Atmosphérique, Université des Sciences et Techniques de Lille, Villeneuve d'Ascq, France.

(Received March 21, 1996; revised December 3, 1996;
accepted December 3, 1996.)